Assessing the effect of chest orientation
on pulmonary pressure under free field shock waves:
a numerical analysis

ZHUANGQING FAN[1, 2], SHUANGBO ZHANG[2], HUIFANG GAN[2], JING CHEN[2], CHANGKAI DAI[2],
BENWEN ZHANG[2], FANGYUN LU[1], JINLONG QIU[2], JIANYI KANG[2]*

[1] College of Science, National University of Defense Technology, Hunan, China.
[2] Daping Hospital, Army Medical Center, Chongqing, China.

Purpose: This study explores how thoracic orientation affects lung pressure and injury outcomes from shock waves, building on earlier research that suggested human posture impacts injury severity. *Methods*: A layered finite element model of the chest was constructed based on the Chinese Visual Human Dataset (CVH), including the rib and intercostal muscle layers. The dynamic response of the chest under 12 different angle-oriented shock waves under incident pressures of 200 kPa and 500 kPa was calculated. The correspondence between lung pressure at various angles, chest wall motion velocity and lung stress, and differences in pressure/stress of lung tissue behind ribs and intercostal muscle were analyzed. *Results*: The dynamic response of the chest can be roughly divided into four processes. High local intrapulmonary pressure areas were primarily in the anterior lobe margin and the lung's central region. A 500 kPa incident wave at 0° could cause slight lung injury, whereas at 240°, the pressure was non-harmful. Lung tissue pressure and stress induced by chest wall movement were significantly higher behind the intercostal muscles than behind the ribs, with a difference of about 2–3 times. *Conclusions*: This layered model provides a cost-effective tool for large-scale shock wave impact simulations on the chest. Chest wall movement velocity strongly correlates with lung stress distribution. The significant density and sound velocity differences among ribs, intercostal muscles and lungs cause an acoustic impedance mismatch, leading to "striped bleeding" marks in post-impact lungs. This research enhances understanding of chest and lung injury mechanisms and informs the development of protective measures.

Key words: blast injury, chest orientation, intrapulmonary pressure, numerical analysis

1. Introduction

The lungs are ones of the most vulnerable organs in the human body under the blast shock wave [17]. When a shock wave impacts the human chest, it forms stress waves that propagate through the lung tissues, leading to the rupture of alveoli and capillaries, which results in pulmonary hemorrhage and edema [24], [25]. To predict and evaluate human lung injury, Bowen et al. [6] established an injury criterion based on the damage test data of more than 1000 mammals across 13 species exposed to explosions and shock tubes, with loading described by the positive phase duration and peak overpressure. Bass et al. [4] suggested that Bowen's curve overestimated injury during the short pulse phase and modified the model. Axelsson et al. [2] developed an injury predictor that takes the speed of chest wall movement as the main index and does not consider the animal's orientation. Later, Stuhmiller et al. [32] proposed a blast injury model that established a damage model based on the normalized work (dimensionless quantity) received by the lungs. The model considered the orientation of the front, left and right directions of the personnel, but the difference in damage caused by the orientation remains unclear.

In recent years, finite element numerical simulation has emerged as a very effective method for studying

the damage mechanism and response process of impact injuries [7], [26]. Roberts and Chen [28] developed the world's first finite element model of the human chest, which laid the foundation for numerical simulation of the human body. A.D. Greer [12] developed a lamellar finite element model between the 5th and 6th layers of the human thoracic vertebrae and analyzed the differences between different evaluation models. Kang et al. [19] built a finite element model of the human chest based on the Chinese Visual Human Dataset by using the MIMICS 3D reconstruction model and studied the dynamic process of the shock wave effect on the chest. Tang et al. [34] constructed a finite element model of the human chest to study the problems related to the interaction of shock waves and fragments. The studies above have not reported much on the effect of human body orientation on shock waves.

On a battlefield or at the site of an explosion, it is observed that individuals at the same distance from the source of the explosion can suffer varying degrees of harm [15]. This variability in injury outcomes can be attributed, in part, to individual differences in height and weight [39]. Additionally, the orientation of the body at the time of the explosion plays a significant role [31]. Previous research by Bowen [6] and Stuhmiller et al. [32] has considered the impact of human orientation on injury severity when exposed to a shock wave. However, the extent of these differences and the underlying reasons remain unclear. This study carries out a numerical simulation analysis on the effects of varying orientations of the human body facing the shock wave front, with the long axis of the human body perpendicular to the direction of shock wave propagation. Based on the 50th percentile Chinese Visual Human Dataset [41], this paper constructs a finite element model of the region between the 5th and 6th layers of the thoracic vertebrae. The results obtained for lung pressure under a shock wave at different chest orientations provide strong support for developing personnel injury protection and evaluation standards.

2. Materials and methods

2.1. Establishment of finite element model

The main steps of the model's construction and calculation are as follows:

1) Convert the photos between the 5th and 6th thoracic vertebrae into grayscale images, and identify the boundaries of different tissues and organs according to the gray value (Fig. 1);
2) Import the grayscale images into the MIMICS 3D software to generate the geometric of the chest between the 5th and 6th thoracic vertebrae;
3) Import the reconstructed geometric into LS-PREPOST software to mesh, to set the contact mode between tissues and organs, to select the material model, and input the material parameters;
4) Generate Keywords and import them into LS-DYNA solver to calculate the dynamic response.

The 50th percentile Chinese Visual Human Dataset (CVH) was developed by the Third Military Medical University. The data were obtained from a 35-year-old adult male (height: 170 cm, weight: 65 kg). The photos selected between the 5th and 6th thoracic vertebrae include the largest cross-sectional area of the lung, sternum, heart, ribs and other important thoracic tissues. This selection facilitates the study of stress wave transmission and tissue response patterns.

The finite element model established in this study draws upon the models constructed by Greer [12], Thom [35] and Josey [18]. Given that visualization photos are horizontal plaines that pass through multiple ribs and intercostal muscles in the chest rib cage, a simplified assumption is made that the ribs and intercostal muscles are distributed horizontally in the plane. This assumption facilitates the study of load propagation characteristics in the chest wall and lungs. The model consists of two layers: the first layer represents half of the intercostal muscle, while the second layer
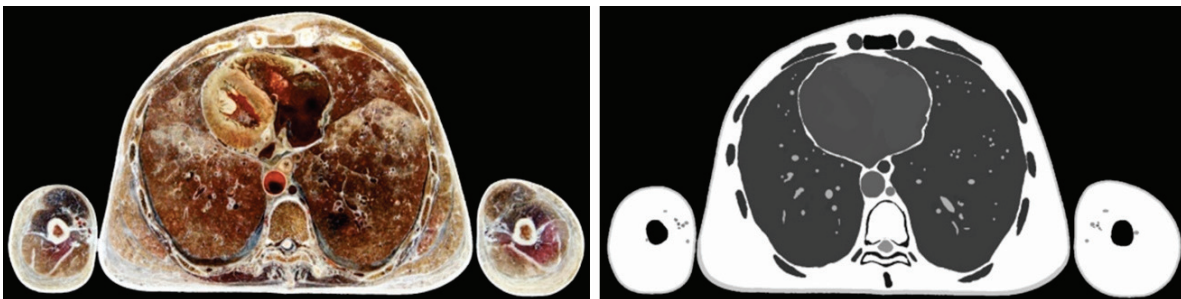

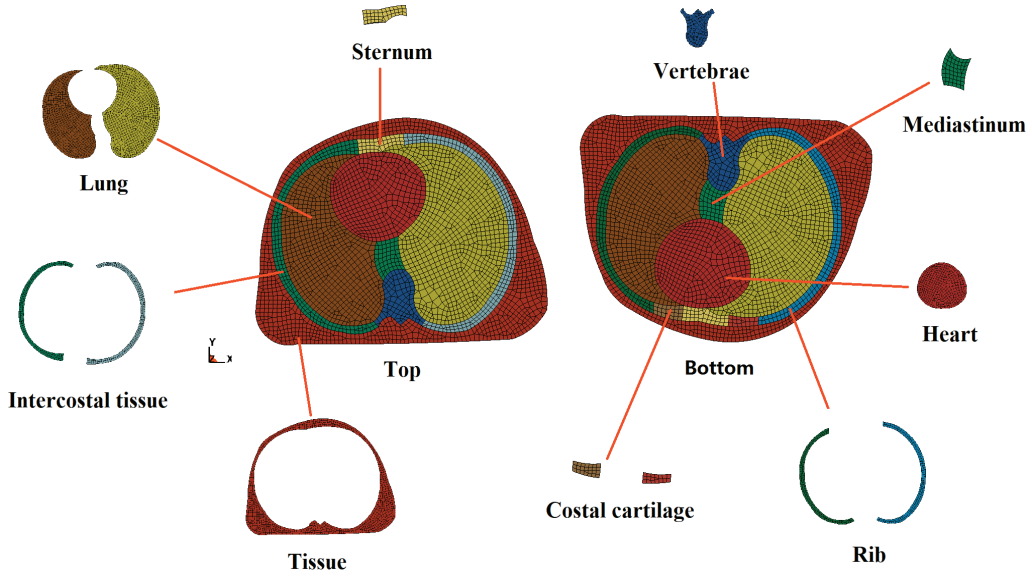Fig. 1. Human body visualization photos and grayscale images
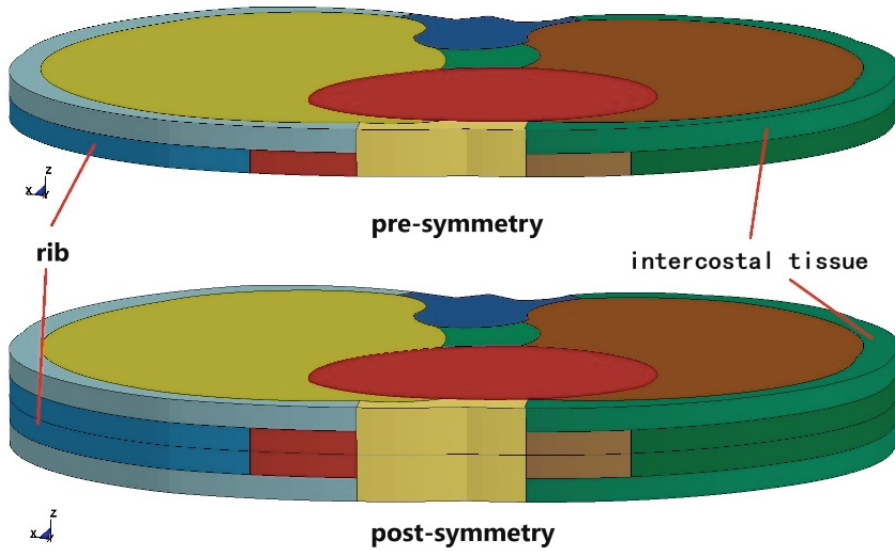
Fig. 2. Chest finite element model

Fig. 3. Finite element symmetric modeling of the chest

represents half of the rib (Fig. 2). Symmetric constraints are applied to the upper and lower surfaces, as depicted in Fig. 3.

2.2. Material models and parameters

2.2.1. Air models and parameters

The NULL material model is selected for air, in which equations of state (EOS) are described by the ideal gas EOS (*EOS_IDEAL_GAS) [33]. A high-pressure zone is established at the edge of the air domain, in the form of high-pressure gas release, to simulate the shock wave caused by the explosion, as shown in Fig. 4a. This is achieved by modifying the initial temperature setting in the EOS. The pressure control equation in the ideal gas EOS is as follows:

$$p = \rho(C_p - C_v)T, \tag{1}$$

where p is the initial pressure, ρ is the air density, C_p is the specific heat at constant pressure, C_v is the specific heat at constant volume, and T is the temperature. The material parameters are shown in Table 1.

Table 1. Air material parameter

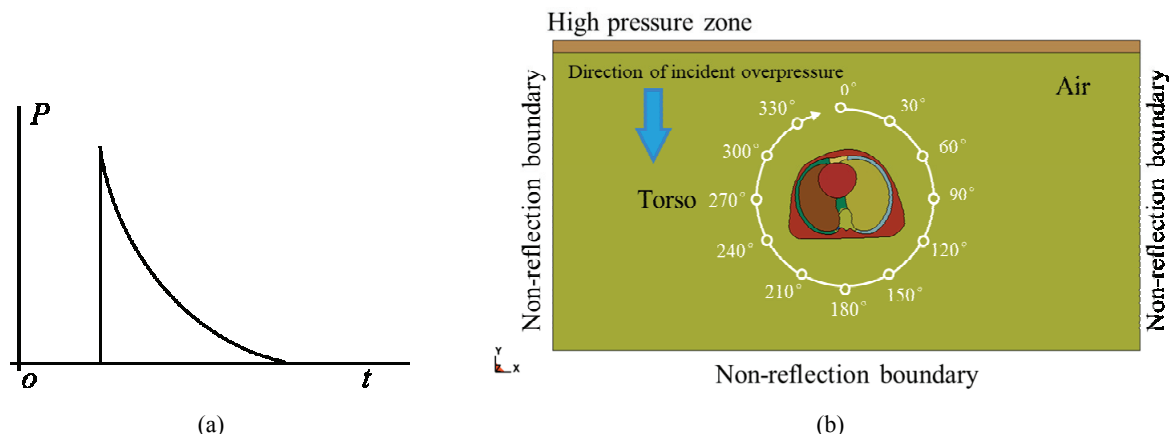| Material	ρ [kg/m^3]	C_p [J/(kg·K)]	C_v [J/(kg·K)]	T [K]	Relative volume
Air	1.293	1005	718	270	1

Fig. 4. Model configuration. (a) Simulated overpressure curve, (b) overall model of the torso and air

2.2.2. Bone and cartilage material models and parameters

The microscopic bone structure comprises the outer cortical bone and the inner cancellous bone. To simplify the calculations, the distinction is no longer made between the two, but the average value of their parameters [22]. Given that a simple shock wave does not cause rib fractures, both bone and cartilage tissues are described using an elastic material model and the Gruneisen equation of state [30]. Notably, there are significant differences in parameters such as density, elastic modulus, and volume modulus between them, as shown in Table 2 [9].

Table 2. Bone and cartilage material parameters

Part	Density [kg/m]	Young's modulus [GPa]	Poisson's ratio	Sound speed [m/s]
Rib	1561	7.92	0.379	3073
Sternum	1354	3.51	0.387	2248
Spine	1644	9.68	0.376	3282
Cartilage	1281	0.049	0.400	286

2.2.3. Muscle and heart material models and parameters

Muscles, heart and other tissues possess complex microstructures, including fiber bundles with directional characteristics, and exhibit both elastic and viscous properties at the macro level [1]. The heart is a hollow structure filled with blood, and there is a significant difference in their properties. In this model, the heart is simplified as a uniform material, and the viscoelastic material model is used to represent the heart and other organs such as muscles and soft tissues [3]. Given the differences in characterization, the relevant parameters vary, as shown in Table 3.

Table 3. Muscle and other soft tissue material parameters

Part	Density [kg/m^3]	Sound speed [m/s]	Bulk modulus [N/m^2]
Muscle	1000	1500	2.2×10^9
Heart	1050	1540	2.2×10^9

2.2.4. Pulmonary material model and parameters

The lung poses the greatest challenge in characterizing chest tissue due to its complex microstructure, encompassing numerous alveolar tissues, capillaries, and a high air content [27], [40]. The overall wave velocity of the lungs is 30–40 m/s, which is much lower than the wave velocity in air or water, and the deformation of the lungs has extremely nonlinear characteristics [11]. In this study, void materials were used and the Gruneisen EOS to characterize lung materials. The parameters are detailed in Table 4 [5].

Table 4. Lung material parameters

Part	Density [kg/m^3]	Sound speed [m/s]	Dynamic viscosity [Pa·s]
Lung	200	30.5	1.0

2.3. Contact mode, algorithm, and calculation Setting

2.3.1. Elements, grids, algorithms, and contacts

The elements selected in the model are all SOLID164 solid elements. The meshing method uses an adaptive algorithm, with a predominantly 8-node hexahedral mesh and a tetrahedral mesh for the transi-

tion mesh (Fig. 2). The chest model is described using a LAGRANGE grid. The air domain employs the ALE (Arbitrary Lagrangian-Eulerian) algorithm. The impact of incident shock waves on the chest in the air is analyzed using a fluid-structure coupling algorithm (*CONSTRAINED_LAGRANGE_IN_SOLID) [38]. The air domain is the ambient atmospheric pressure and the chest model is placed in the air domain (Fig. 4b). Symmetric constraints are applied to the upper and lower surfaces of the model (Fig. 3), and the air domain's boundary is set as a non-reflective boundary to prevent the wave front's reflection effect. The interaction between the various tissues and organs of the chest is modeled using automatic surface-to-surface contact [37].

2.3.2. Grouping

This study primarily investigates the effects of different angles on pulmonary pressure when the long axis of the body is perpendicular to the direction of shock wave propagation. The incidence direction of the shock wave was maintained constant, with the chest facing the shock wave at an angle of 0°. The model was then incrementally rotated 30° clockwise to obtain the distribution of pulmonary pressure at each corresponding angle (Table 5). For model validation, the modified Bowen model (Bass model) was used [5], selecting the peak overpressure at threshold damage and the 1% fatality rate as incident pressure. The results obtained at 0° angle will be compared with the modified Bowen model to verify the accuracy of our model.

Table 5. Calculationgrouping settings

Incident overpressure [kPa]	Positive phase duration [ms]	Orientations and numbers
200	2	0°, 30°, 60°, ..., 330°, 12 angles in total
500	2	0°, 30°, 60°, ..., 330°, 12 angles in total

3. Results

3.1. Dynamic process of load propagation

The dynamic response of the chest under two incident pressures has been calculated. The dynamic response of the chest oriented at a 0° to an incident overpressure of 200 kPa is illustrated in Fig. 5. The dynamic process can be roughly divided into four stages: first, at 0.5 ms, the shock wave front contacts the chest sur-
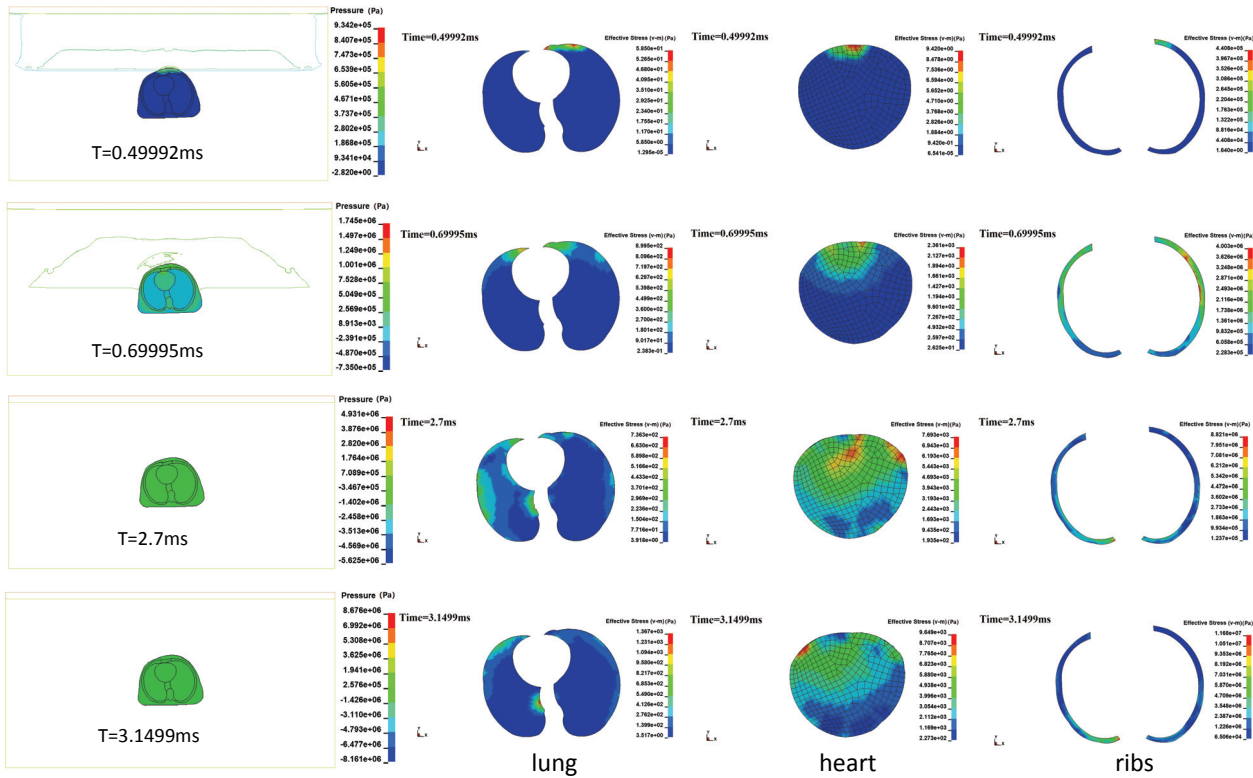

Fig. 5. Pressure and organ stress distribution map at different times for the chest at 0° under the effect of 200 kPa incident pressure

face, triggering a stress response in the soft tissue, lung lobe edges, and rib edges. Second, at 0.7 ms, the shock wave front reaches the middle of the chest, causing continued deformation of the chest's soft tissues and ribs, with stress concentration appearing on the front of the heart and lungs, while the backside remains undisturbed. Third, at 2.7 ms, when the wave front reaches the back of the chest, the organs in the chest activate completely, with a significant increase in stress amplitude compared to the second stage. Finally, at 3.15 ms, even though the shock wave front has moved away from the chest model, the oscillation of the tissues within the chest cavity continues due to inertia and viscosity effects. Throughout the entire process, the highest points of local pressure in the left and right lungs appear at the tip of the lobe edge near the heart, which is consistent with the results showing the distribution of pulmonary hemorrhage along the lobe border.

3.2. Pulmonary pressure distribution at different chest angles

The chest is initially set at a 0° orientation facing the shock wave front, after which the chest orientation is increased clockwise by 30° increments. The intrapulmonary pressure distribution at 12 different orientations under an incident shock wave of 200 kPa at 1.35 ms is illustrated in Fig. 6. It is observable that the pulmonary pressure distribution varies significantly with different orientations at the same moment. The causes for these differences will be discussed and analyzed in the following sections.

3.3. Stress time history curves of different tissues and organs

The chest model oriented at 0° under an incident pressure of 200 kPa is presented in Fig. 7. In the figure the different sections of the lung, heart, ribs and intercostal muscles are highlights, and the stress–time curve for these tissues after exposure to the incident pressure is provided. The time it takes for the stress wave to reach different tissues varies, thus the time for each stress peak also differs. At the selected points in the figure, the maximum stress experienced was 3.5 MPa for the ribs, 0.65 kPa for the lungs, 4 kPa for the heart and 48 kPa for the intercostal muscles.
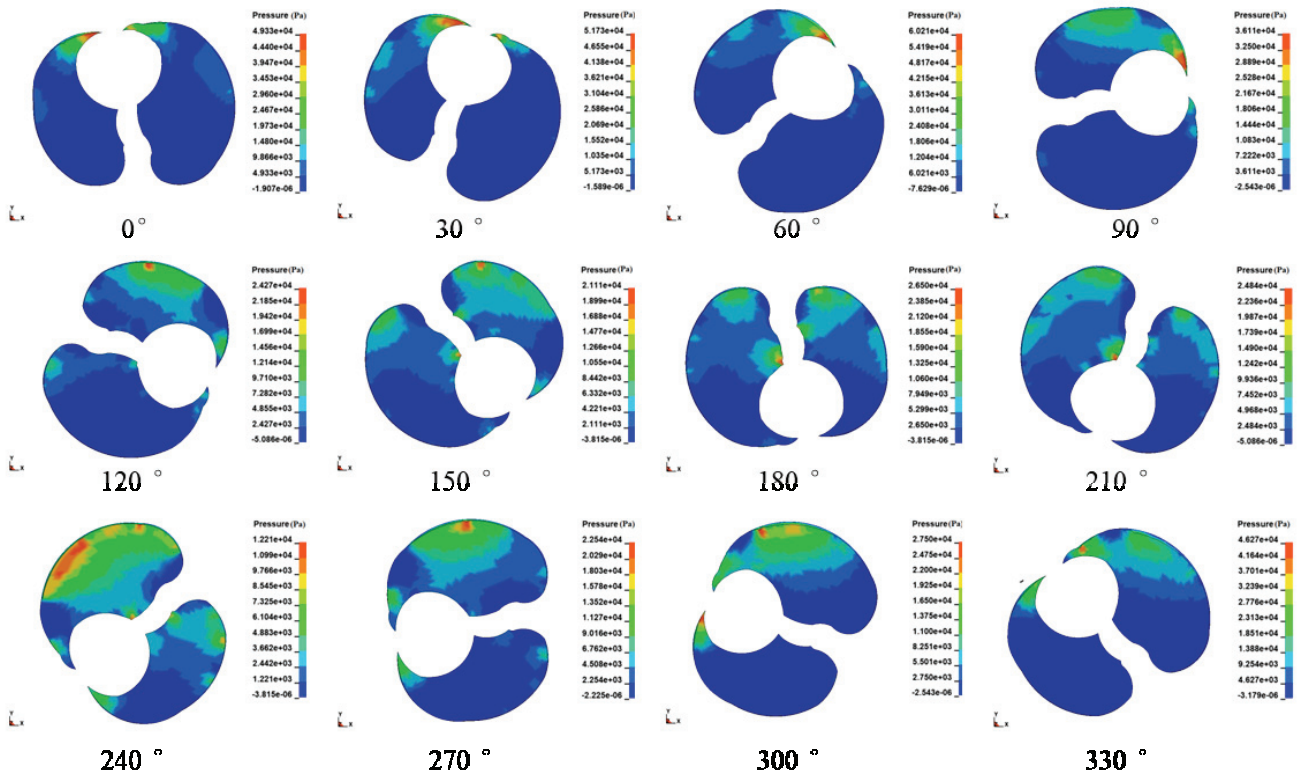

Fig. 6. Lung pressure distribution map at different angles at the 1.35 ms moment for the chest under the effect of 200 kPa incident pressure
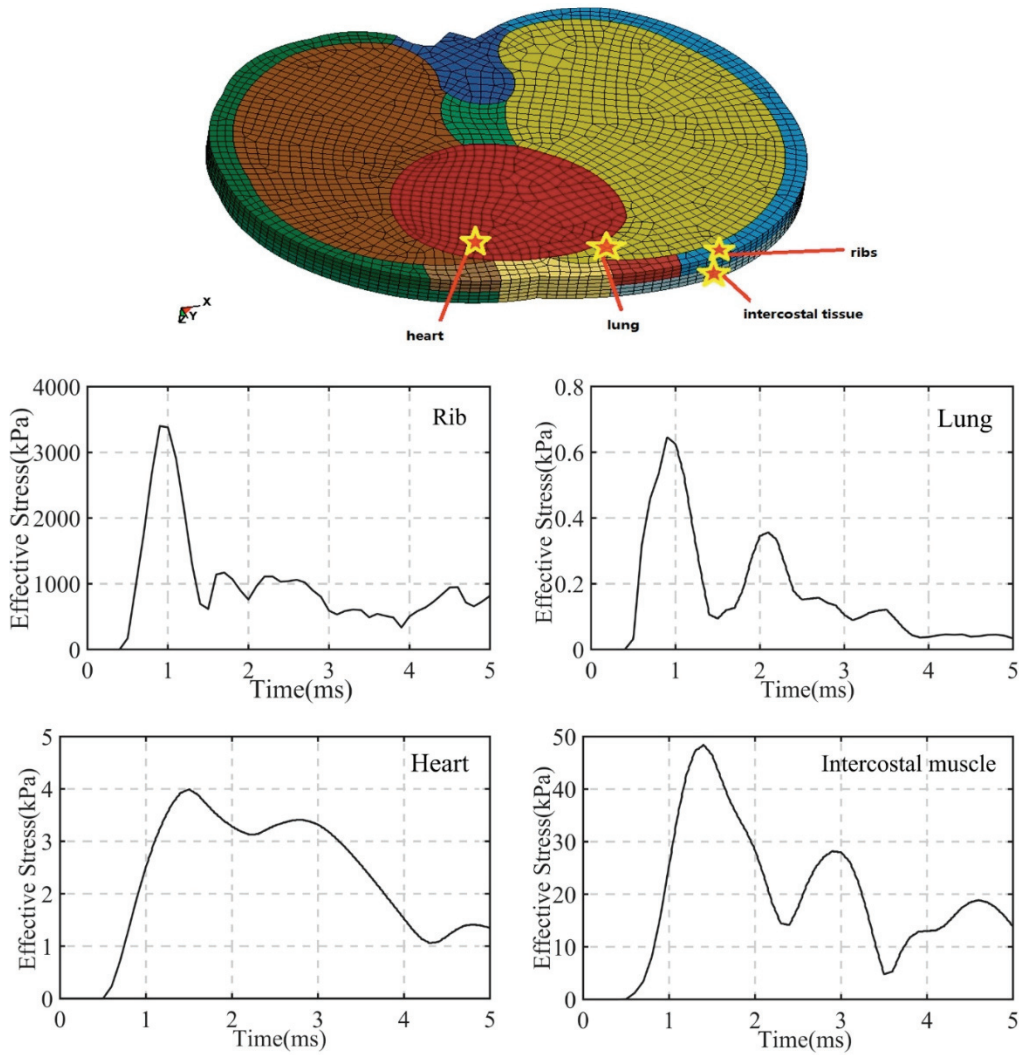
Fig. 7. Stress–time curve of chest tissues at 0° under 200 kPa shock wave loading

4. Discussion

4.1. Model correctness validation

Alexander [12] made a comparison between the modified Bowen curve proposed by Bass, the chest wall motion velocity model proposed by Axelsson and Stuhmiller's normalized work model. He suggested that the peak value of local pressure in the lung was closely related to injury, proposing a threshold for local peak pressure in the lung corresponding to different degrees of injury: no injury (less than 60 kPa), trace injury (60–100 kPa), slight injury (100–140 kPa), moderate injury (140–240 kPa), and severe injury (greater than 240 kPa). In this paper, an incidence pressure of 200 kPa with a duration of 2 ms corresponds to the damage threshold on the Bass curve, while an incident pressure of 500 kPa with a duration of 2 ms corresponds to a 1% mortality rate on the Bass curve [29]. The upcoming comparison of local intrapulmonary pressure will serve to validate the accuracy of the model developed in this study.

In Figure 8, the pressure history of the lung lobe edge under the impact of a 200 kPa incident pressure at a 0° orientation is depicted. The maximum value observed in the figure is 50 kPa, which is less than the damage threshold of 60 kPa, that is, according to the effect of Bass curve on the damage threshold under 200 kPa incident pressure, the maximum pressure area of the whole lung does not exceed the local intrapulmonary pressure damage threshold indicating that no damage would be caused under these conditions. The pressure history of the lung lobe edge when a 500 kPa incident pressure exerted on the chest at a 0° orientation is presented in Fig. 9. In the figure, it is shown that the maximum local intrapulmonary pressure
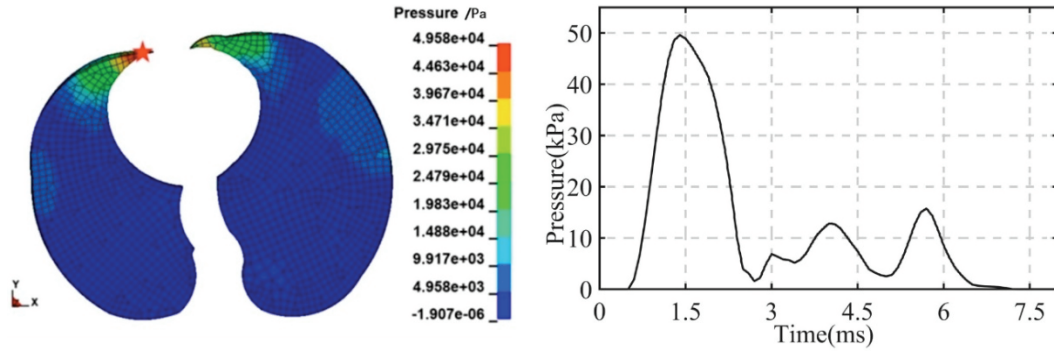
Fig. 8. Pressure curve of the lung lobe margin in a 0° chest orientation under the effect of 200 kPa
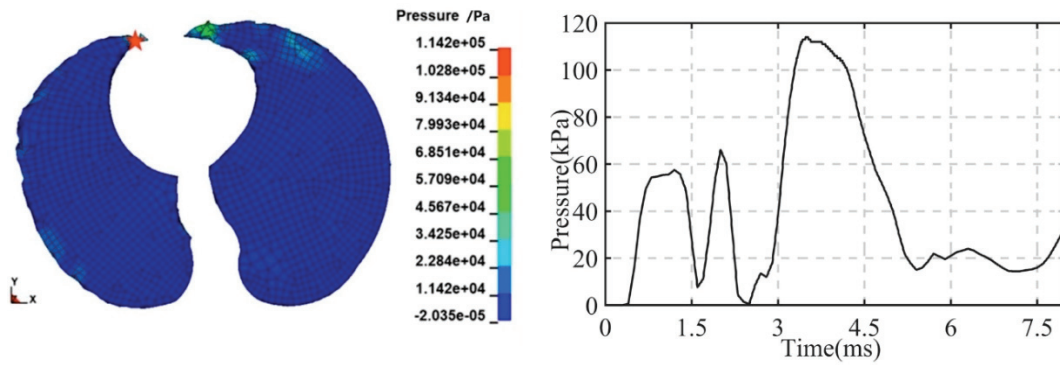

Fig. 9. Pressure curve of the lung lobe margin in a 0° chest orientation under the effect of 500 kPa

reaches 112 kPa, hitting the mild injury threshold of local intrapulmonary pressure (100–140 kPa), which aligns with the Bass curve threshold. The regions of the lungs with high pressure values, as presented in the model in this study, align with the areas of bleeding in the lung lobe margins and other parts, as reported in the literature [16]. Based on the location of local intrapulmonary pressure injury and pressure distribution, the model established in this study can more accurately predict the likelihood of injury and reflect the chest's response under shock wave load.

4.2. Distribution of pulmonary pressure at different angles of the chest

To investigate the impact of various chest orientations on intrapulmonary pressure under the same incident pressure, 12 points within the lung tissue were selected, as depicted in Fig. 10. These points were categorized into three areas: the anterior pulmonary area (points 1, 2, 3, 4), the middle pulmonary area (points 5, 6, 7, 8) and the posterior pulmonary area (points 9, 10, 11, 12). The intrapulmonary pressure values resulting from a 200 kPa incident pressure are displayed in Fig. 11, whereas those resulting from a 500 kPa incident pressure are shown in Fig. 12.

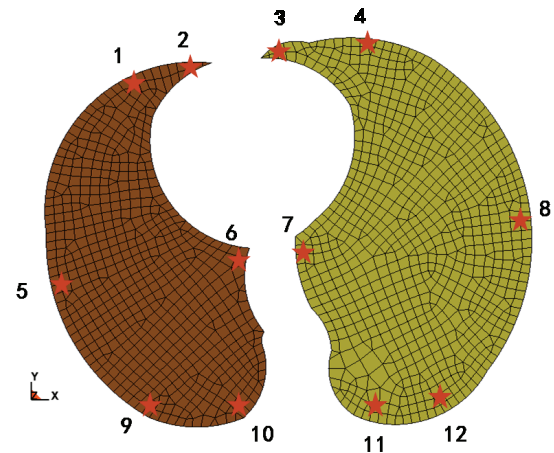Fig. 10. Schematic diagram of pressure measurement points inside the lung

4.2.1. Local maximum pulmonary pressure position difference caused by different orientations

Changes in orientation cause variations in the position of the chest wall impacted by the shock wave, which, in turn, leads to differences in the location of maximum pressure within the lung. The locations of maximum intrapulmonary pressure within the chest

at different orientations under two incident pressures are presented in Table 6 and the position number is consistent with Fig. 10.

In Table 6, it is revealed that the maximum pressure primarily occurs in the anterior lung area when the chest is oriented towards the shock wave array, and predominantly in the middle lung area when the spine is oriented towards the shock wave array. The posterior area of the lungs (points 9, 10, 11, 12), located near the spine, remains largely unaffected regardless of the chest orientation. In refining the injury prediction model, Stuhmiller [23] noted that due to the
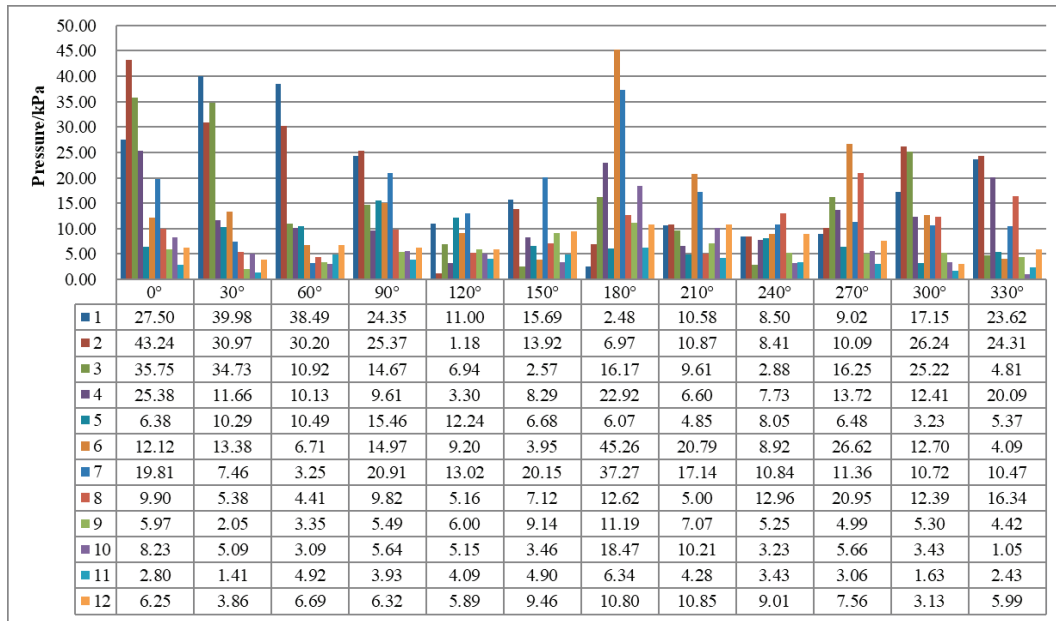

	0°	30°	60°	90°	120°	150°	180°	210°	240°	270°	300°	330°
1	27.50	39.98	38.49	24.35	11.00	15.69	2.48	10.58	8.50	9.02	17.15	23.62
2	43.24	30.97	30.20	25.37	1.18	13.92	6.97	10.87	8.41	10.09	26.24	24.31
3	35.75	34.73	10.92	14.67	6.94	2.57	16.17	9.61	2.88	16.25	25.22	4.81
4	25.38	11.66	10.13	9.61	3.30	8.29	22.92	6.60	7.73	13.72	12.41	20.09
5	6.38	10.29	10.49	15.46	12.24	6.68	6.07	4.85	8.05	6.48	3.23	5.37
6	12.12	13.38	6.71	14.97	9.20	3.95	45.26	20.79	8.92	26.62	12.70	4.09
7	19.81	7.46	3.25	20.91	13.02	20.15	37.27	17.14	10.84	11.36	10.72	10.47
8	9.90	5.38	4.41	9.82	5.16	7.12	12.62	5.00	12.96	20.95	12.39	16.34
9	5.97	2.05	3.35	5.49	6.00	9.14	11.19	7.07	5.25	4.99	5.30	4.42
10	8.23	5.09	3.09	5.64	5.15	3.46	18.47	10.21	3.23	5.66	3.43	1.05
11	2.80	1.41	4.92	3.93	4.09	4.90	6.34	4.28	3.43	3.06	1.63	2.43
12	6.25	3.86	6.69	6.32	5.89	9.46	10.80	10.85	9.01	7.56	3.13	5.99

Fig. 11. Pressures at 12 points at different angles under an incident pressure of 200 kPa

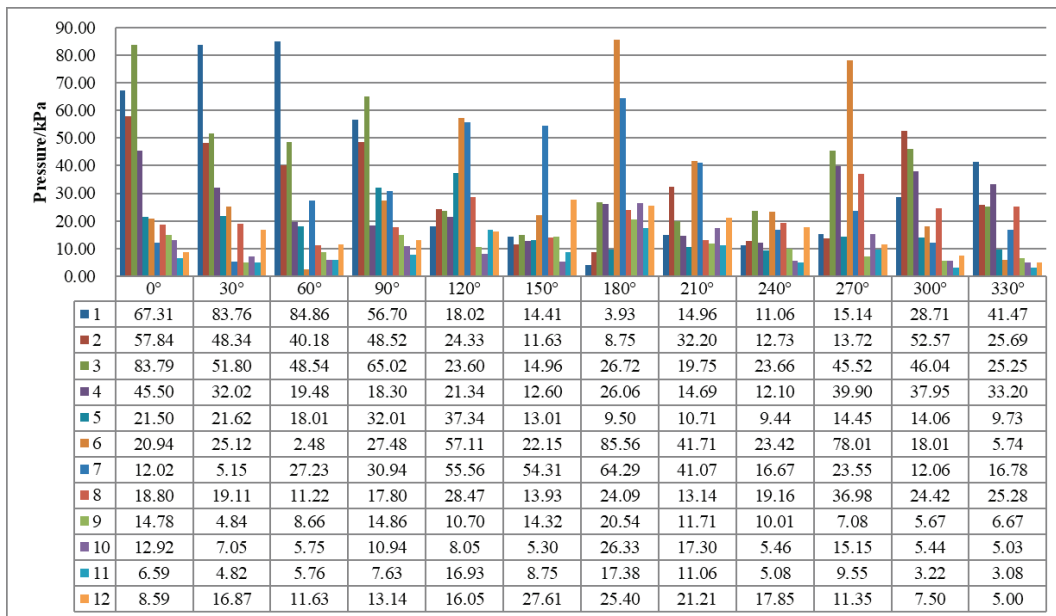|	0°	30°	60°	90°	120°	150°	180°	210°	240°	270°	300°	330°
1	67.31	83.76	84.86	56.70	18.02	14.41	3.93	14.96	11.06	15.14	28.71	41.47
2	57.84	48.34	40.18	48.52	24.33	11.63	8.75	32.20	12.73	13.72	52.57	25.69
3	83.79	51.80	48.54	65.02	23.60	14.96	26.72	19.75	23.66	45.52	46.04	25.25
4	45.50	32.02	19.48	18.30	21.34	12.60	26.06	14.69	12.10	39.90	37.95	33.20
5	21.50	21.62	18.01	32.01	37.34	13.01	9.50	10.71	9.44	14.45	14.06	9.73
6	20.94	25.12	2.48	27.48	57.11	22.15	85.56	41.71	23.42	78.01	18.01	5.74
7	12.02	5.15	27.23	30.94	55.56	54.31	64.29	41.07	16.67	23.55	12.06	16.78
8	18.80	19.11	11.22	17.80	28.47	13.93	24.09	13.14	19.16	36.98	24.42	25.28
9	14.78	4.84	8.66	14.86	10.70	14.32	20.54	11.71	10.01	7.08	5.67	6.67
10	12.92	7.05	5.75	10.94	8.05	5.30	26.33	17.30	5.46	15.15	5.44	5.03
11	6.59	4.82	5.76	7.63	16.93	8.75	17.38	11.06	5.08	9.55	3.22	3.08
12	8.59	16.87	11.63	13.14	16.05	27.61	25.40	21.21	17.85	11.35	7.50	5.00

Fig. 12. Pressures at 12 points at different angles under an incident pressure of 500 kPa

Table 6. Position of maximum pressure at each orientation

Orientation	0°	30°	60°	90°	120°	150°	180°	210°	240°	270°	300°	330°
200 kPa	2	1	1	2	7	7	6	6	8	6	2	2
500 kPa	3	1	1	3	6	7	6	6	3	6	2	1

stiffness of the spine region, it undergoes essentially no significant deformation. In the process of calculating normalized work in different directions, using Stuhmiller's model, the coefficient of the chest anterior region is 0.5, and the coefficients of the left and right sides of the chest wall are 0.25, respectively, and the spinal region is not involved in the calculation. The calculations in this study indicate that the baseline pressure of the lung tissue near the spine changes the least, which validates the appropriateness of Stuhmiller's modified model that excludes the coefficient for the back.

4.2.2. Difference of mean pulmonary pressure at different angles

The pressure values at the 12 points depicted in Fig. 10 were averaged for the anterior, middle and posterior sections of the lung as well as for the whole lung.
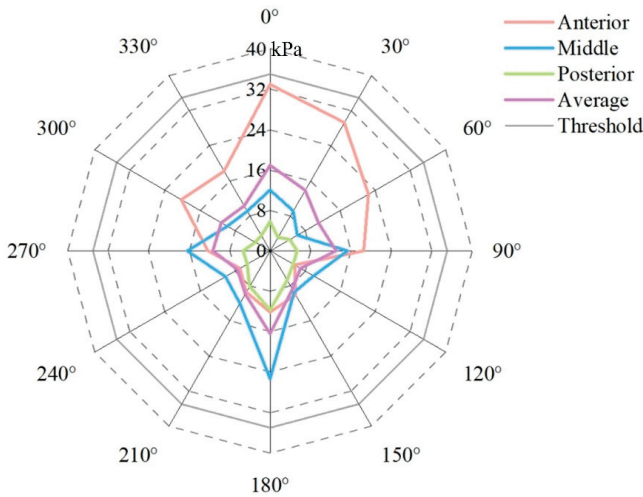
Fig. 13. Difference in average lung pressure at different angles under the effect of 200 kPa incident pressure
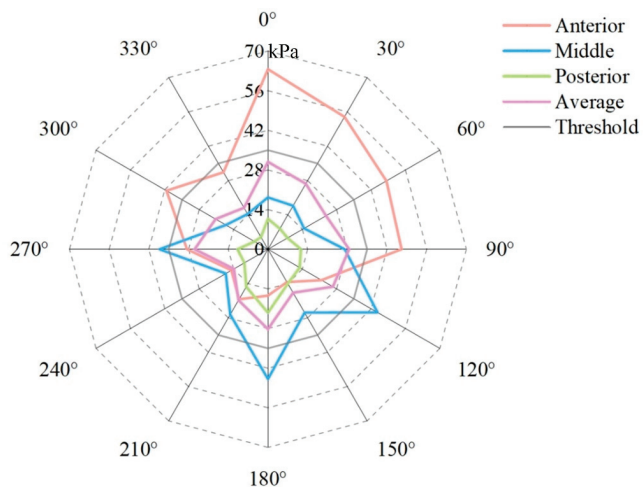
Fig. 14. Difference in average lung pressure at different angles under the effect of 500 kPa incident pressure

The average values for these four groups were subsequently represented in the form of radar line charts, differentiated by various angles. The distribution under an incident pressure of 200 kPa is illustrated in Fig. 13, whereas distribution under an incident shock wave pressure of 500 kPa is depicted in Fig. 14.

Analysis from different angles revealed that when the chest is oriented between 300° and 90°, the local pressure at the front of the lung is higher than in other parts. The pressure in the middle of the lung is higher than in other parts when the chest faces between 90° and 270°. When the chest is oriented at an angle of 240°, all parts of the lungs experience the least pressure, with the difference between the front, middle and back of the lungs, and the average pressure being 2–5 times. According to the criterion for average intrapulmonary pressure injury, the injury threshold is 35 kPa and the slight injury threshold is 60 kPa [12]. Under an incident pressure of 500 kPa, slight injury occurs when the chest is oriented to 0°, whereas injury can be avoided when the chest is oriented to 240°.

For the anterior pulmonary pressure, under 200 kPa incident pressure, the pulmonary pressure at 0° is less than 35 kPa, and the minimum average anterior pulmonary pressure is approximately 5 kPa at 120° and 240°. Under 500 kPa, the average maximum anterior pulmonary pressure is close to 70 kPa, reaching the slight injury threshold, and the minimum is approximately 15 kPa at 150° and 240°.

For the average pressure in the middle part of the lung, when the incident pressure is applied at 200 kPa, the maximum value is 25 kPa at 180°, the average value is 7 kPa at 60°, and the maximum and minimum angles of 200 kPa remain the same at 500 kPa. The maximum and minimum values at 500 kPa are 50 kPa and 15 kPa, respectively.

For the posterior part of the lung, the average pressure following the two incident overpressures was lower than that in other parts, which aligns with our previous analysis results. At a 0° angle, this area was the last to be disturbed, and at 180°, there was almost no inward movement due to the high rigidity of the spine.

4.2.3. Analysis of reasons for difference of average pulmonary pressure caused by orientation

(1) Differences in Effective Area: Regardless of the model in question – be it Bowen, Axelsson [2] or Stuhmiller [32] – the chest is conceptualized as a single piston model. The shock wave-affected area of the chest wall is a crucial parameter in all these models. As the

angle of the chest rotates, the area of the chest wall directly influenced by the shock wave changes, leading to variations in lung pressure. (2) Differences in Rib Cage Strength: The rib cage of the chest, bearing an oval shape, exhibits varying strengths in different directions. The posterior ribs, connecting to the spine, possess the highest strength, whereas the anterior part – aligned with the largest area of the "oval" – exhibits less strength.

4.3. Correlation analysis of rib velocity, intercostal muscle velocity and high value area of lung stress

Shock wave loads apply force on the chest wall, causing an inward acceleration and subsequent impact on the lungs. Based on this concept, Axelsson [2] developed a physical model that establishes a correlation between the velocity of chest wall movement and the severity of the resultant injury.

The model developed in this study calculates the velocity history of rib and intercostal muscle elements in the chest wall following a 500 kPa incident pressure load on the chest (Fig. 15). The velocity changes in the intercostal muscle tissue and rib tissue were similar, indicating that the surface of the chest wall moves as a unit under the influence of a shock wave, with a velocity of 8 m/s. When compared with Axelsson's chest wall velocity and injury correspondence scale, it was found that the lung injury ranged from light to moderate [20], which was in line with the expected results.

stress peak occurring at 1ms and the second peak at 3 ms. This pattern reflects the foam-like properties of the pulmonary material [8].

Fig. 16. Effective stress history curve of the right lung in contact with the intercostal muscles under the effect of 500 kPa incident pressure

4.4. Differences in lung tissue pressure/stress after rib and intercostal muscle

As described in Section 2.1, the model developed in this paper bifurcates the chest into two layers: the costal (rib) layer and the intercostal muscle layer. The movement of the chest wall engenders stress waves [10], thereby escalating the pressure and stress on the lungs. However, the ribs and intercostal muscles of the chest wall exhibit significant differences
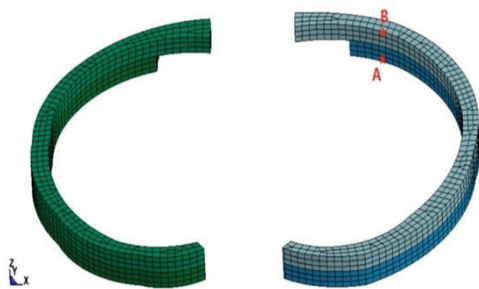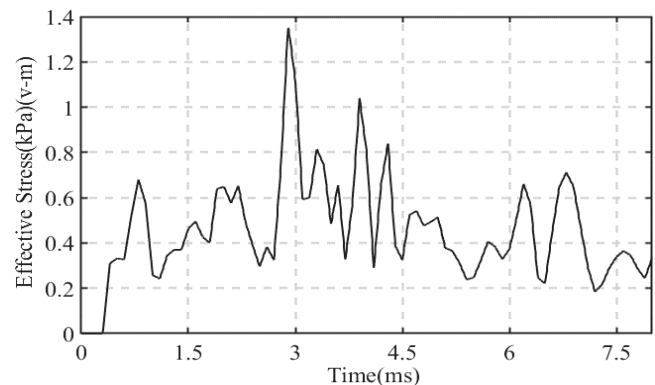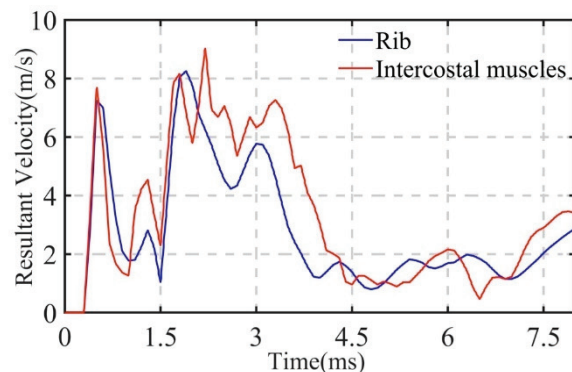

Fig. 15. Velocity history curve of the right ribs and intercostal muscles under the effect of 500 kPa incident pressure

Upon examining the pulmonary stress curve after the action of the intercostal muscle (as depicted in Fig. 16), it was observed that the chest wall's movement velocity peaked at 0.5 ms and exhibited a secondary peak at 2 ms. Correspondingly, the peaks in the pulmonary pressure history were delayed, with the first

due to variations in material density and sound velocity. This study zeroes in on lung tissue elements situated behind the rib and intercostal muscles, subjected to an incident pressure of 500 kPa (illustrated in Fig. 17). It this figure, the tissue stress and pressure curves (portrayed in Fig. 18) one juxtaposed,

while in Fig. 19, the pressure history of the right lung is delineated.

In the figures, a significant discrepancy between the pressure and stress values of the lung tissue situated behind the rib and the intercostal muscle is unveiled. According to the analysis in Section 4.3 (Fig. 15), the velocities of the rib and intercostal muscle are fundamentally identical. However, the pressure and stress exerted on the lung tissue behind the intercostal mus-

cle surpass those on the lung tissue surface behind the rib. This discrepancy directly instigates the "striped bleeding" or "intercostal bleeding" observed in the lung blast injury [21].

The lung injury stemming from the overall movement of the chest wall is ascribed to the acoustic impedance mismatch at the interface [13], [14]. The product of sound velocity and density (acoustic impedance) of the ribs, intercostal muscles and lungs exhibits signifi-
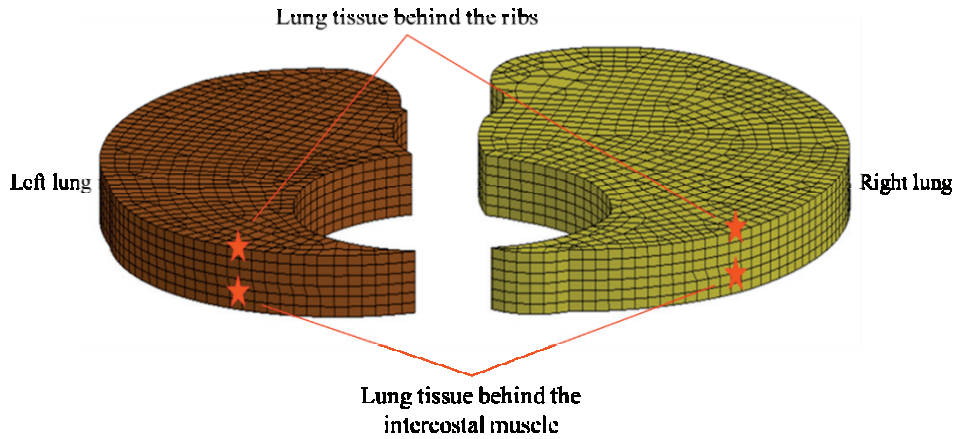

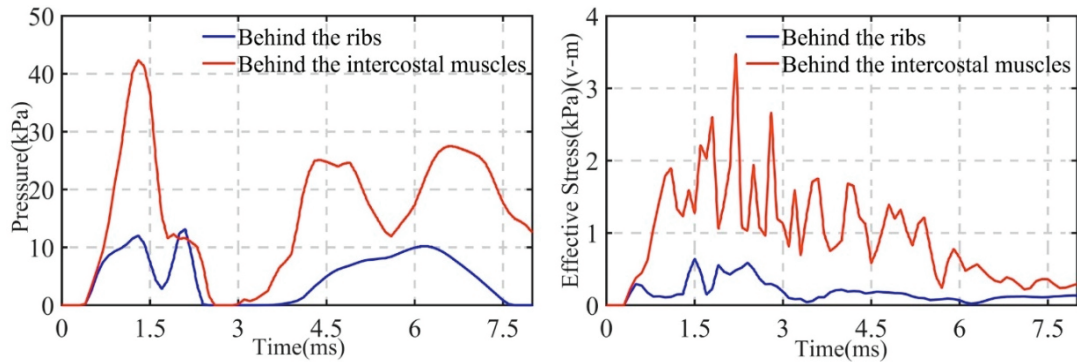Fig. 17. Selection of points in the lung behind the ribs and intercostal muscles

Fig. 18. Comparison of pressure and stress history in the left lung element
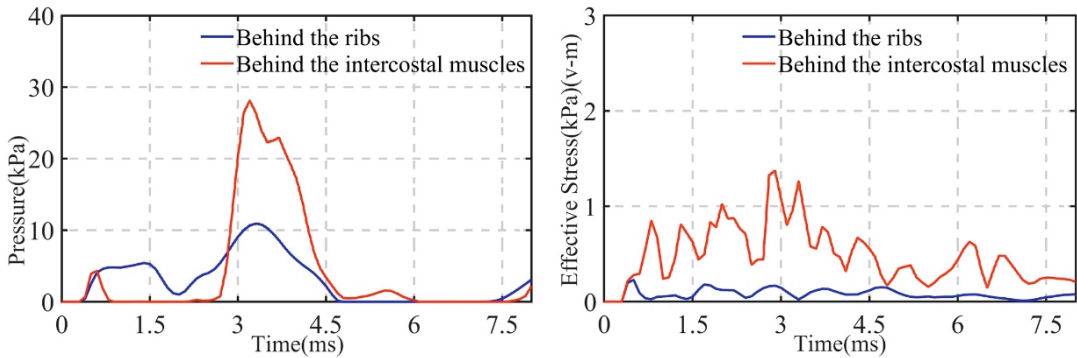

Fig. 19. Comparison of pressure and stress history in the right lung element

cant variation, culminating in differences in the pressure and stress exerted on the lung surface [36]. Due to the compression and shear forces, the lung manifests "striped bleeding" marks. The theoretical analysis here will be emphasized in other subsequent articles.

5. Conclusions

This study constructed a layered chest finite element model based on CVH Dataset and calculated the dynamic response of the chest in 12 different orientations towards a shock wave under incident pressures of 200 kPa and 500 kPa. The research involved an analysis of the pulmonary pressure in various orientations, the correlation between the chest wall's movement velocity and the stress within the lung, and the differences in pulmonary pressure and stress behind the ribs and intercostal muscles.

Key findings include the following:

1) the model accurately reproduces the dynamic response history of the chest, offering a cost-effective and convenient method for large-scale shock wave chest calculations;

2) the overall movement speed of chest wall is strongly related to the stress distribution in the lung, but the load has hysteresis, which is related to the foam-like characteristics of lung materials;

3) the paper provides the relationship between the local pressure in the lung, the mean pressure, and orientation when the chest is facing the shock wave at 12 different orientations, at 0°, the local intrapulmonary pressure in the anterior part of the lung is the highest, while at 240°, both local and average intrapulmonary pressure are the lowest. The high-value locations of local pressure in the lung at different orientations align well with results in existing literature;

4) the density and sound velocity of materials in the ribs, intercostal muscles, and lungs differ greatly. Due to the mismatch in acoustic impedance, the pressure/stress of the lung tissue behind the ribs and intercostal muscles differs 2–3 times. The pressure and stress of the lung tissue behind the intercostal muscles are much greater than those behind the ribs, which is the main reason for the appearance of "striped bleeding" marks in the lungs after blast injury.

This research method and its results offer support for large-scale numerical calculations of chest injuries and can serve as reference for research on the mechanism and protection of chest injuries.

Acknowledgements

References

[1] ANDRIKAKOU P., VICKRAMAN K., ARORA H., *On the behavior of lung tissue under tension and compression*, Sci. Rep., 2016, 6, 36642.

[2] AXELSSON H., YELVERTON J.T., *Chest wall velocity as a predictor of nonauditory blast injury in a complex wave environment*, J. Trauma, 1996, 40 (3 Suppl), S31–37.

[3] BAO Z.Y., *Study on dynamic mechanical properties of biological soft tissue*, Dissertation, Nanjing University of Science and Technology, 2019.

[4] BASS C.R., RAFAELS K.A., SALZAR R.S., *Pulmonary Injury Risk Assessment for Short-Duration Blasts*, J. Trauma, 2008, 65 (3), 604–615.

[5] BHANA R.H., MAGAN A.B., *Lung Mechanics: A Review of Solid Mechanical Elasticity in Lung Parenchyma*, J. Elast., 2023, 153 (1), 53–117.

[6] BOWEN I.G., FLETCHER E.R., RICHMOND D.R., *Estimate of man's tolerance to the direct effects of air blast*, Dissertation, Lovelace Foundation for Medical Education and Research, 1968.

[7] CARMO G.P., DYMEK M., PTAK M., ALVES_DE_SOUSA R.J., FERNANDES F.A.O., *Development, Validation and a Case Study: The Female Finite Element Head(FeFEHM)*, Comput. Methods Programs Biomed., 2023, 231, 107430, DOI: 10.1016/j.cmpb.2023.107430.

[8] CLAYTON J.D., *Modeling lung tissue dynamics and injury under pressure and impact loading*, Biomech. Model Mechanobiol., 2020, 19 (6), 2603–2626.

[9] CLEMEDSON C., JÖNSSON A., *Transmission and Reflection of High Explosive Shock Waves in Bone*, Acta Physiol. Scand., 1961, 51, 47–61.

[10] COOPER G.J., TOWNEND D.J., CATER S.R., PEARCE B.P., *The role of stress waves in thoracic visceral injury from blast loading: Modification of stress transmission by foams and high-density materials*, J. Biomech., 1991, 24 (5), 273–285.

[11] FUNG Y.C., YEN R.T., TAO Z.L., LIU S.Q., *A hypothesis on the mechanism of trauma of lung tissue subjected to impact load*, J. Biomech. Eng., 1988, 110 (1), 50–56.

[12] GREER A.D., *Numerical Modeling for the Prediction of Primary Blast Injury to the Lung*, Dissertation, The University of Waterloo, 2007.

[13] GRIMAL Q., NAILI S., WATZKY A., *A study of impact wave propagation in the thorax*, Mech. Res. Commun., 2002, 29 (2), 73–80.

[14] GRIMAL Q., WATZKY A., NAILI S., *A one-dimensional model for the propagation of transient pressure waves through the lung*, J. Biomech., 2002, 35 (8), 1081–1089.

[15] HSU Y., HO K., CHAN P., *Anthropomorphic Blast Test Device for Primary Blast Injury Risk Assessment*, Mil. Med., 2020, 185 (Suppl. 1), 227–233.

[16] HUANG J.D., YANG Z.H., WANG Z.G., *Morphological changes of the lungs after blast, shell-fragment, and blast-*

fragment combined injuries in dogs, Journal of Army Medical University, 1992, 14 (2), 155–158.

[17] JIANG J.X., ZENG L., *Advance of protection and mechanism of lung blast injury*, Journal of Army Medical University, 2022, 44 (5), 395–398.

[18] JOSEY T., *Investigation of Blast Load Characteristics on Lung Injury*, Dissertation, The University of Waterloo, 2010.

[19] KANG J.Y., WANG J.M., YU Y., M., LI B.C., CHEN J., LIU H., *Biological Effect and Numerical Simulation Study of Complex Blast Wave*, Journal of Army Medical University, 2011, 33 (2), 173–176.

[20] LAUV. K., VIANO D.C., *Influence of impact velocity and chest compression on experimental pulmonary injury severity in rabbits*, J. Trauma, 1981, 21 (12), 1022–1028.

[21] LEWIS B.T., HERR K.D., HAMLIN S.A., HENRY T., LITTLE B.P., NAEGER D.M., HANNA T.N., *Imaging Manifestations of Chest Trauma*, Radiographics, 2021, 41 (5), 1321–1334.

[22] LI X., CHEN L., ZHANG Q.M., ZHANG A.F., MA G., *Research on shock compression test of pigs lower limb*, China Measurement and Test, 2016, 42 (10), 63–67.

[23] MACFADDEN L., CHAN P., HO K., STUHMILLER J., *A model for predicting primary blast lung injury*, J. Trauma Acute Care Surg., 2012, 73 (5), 1121–1129.

[24] MARRO A., CHAN V., HASS B., DITKOFSKY N., *Blunt chest trauma: classification and management*, Emerg. Radiol., 2019, 26 (5), 557–566.

[25] MAYORGA M.A., *The pathology of primary blast overpressure injury*, Toxicology, 1997, 121 (1), 17–28.

[26] NIE J., LV X., HUANG X., LI K., LI G., *Pedestrian dynamic response and injury risk in high speed vehicle crashes*, Acta Bioeng. Biomech., 2022, 24 (3), 56–57.

[27] RICE D., *Sound speed in pulmonary parenchyma*, J. Appl. Physiol., 1983, 54 (1), 304–308.

[28] ROBERTS S.B., CHEN P.H., *Electrostatic analysis of the human thoracic skeleton*, J. Biomech., 1970, 3 (6), 527–545.

[29] SCOTT T.E, KIRKMAN E., HAQUE M., GIBB I.E., MAHONEY P., HARDMAN J.G., *Primary blast lung injury – a review*, Br. J. Anaesth., 2017, 118 (3), 311–316.

[30] SHEN J., ROTH S., *Effect of geometrical and mechanical parameters of ribs submitted to high velocity impact. A numerical investigation*, Mechanics of Advanced Materials Structures, 2022, 29 (25), 4096–4109.

[31] STOTTMEISTER A., VON RAMIN M., SCHNEIDER J.M., *On models of blast overpressure effects to the thorax*, SN Appl. Sci., 2020, 2 (12), 2076.

[32] STUHMILLER J.H., HO K.H., VAN DER VORST M.J., DODD K.T., FITZPATRICK T., MAYORGA M., *A model of blast overpressure injury to the lung*, J. Biomech., 1996, 29 (2), 227–234.

[33] TAN X.G., PRZEKWAS A.J., GUPTA R.K., *Computational modeling of blast wave interaction with a human body and assessment of traumatic brain injury*, Shock Waves, 2017, 27, 889–904.

[34] TANG F., *Research on Human Torso Injury and Protection under Blast wave and Fragment*, Dissertation, Beijing Institute of Technology, 2019.

[35] THOM C.G., *Soft Materials under Air Blast Loading and Their Effect on Primary Blast Injury*, Dissertation, The University of Waterloo, 2009.

[36] WAGNER R.B., JAMIESON P.M., *Pulmonary contusion. Evaluation and classification by computed tomography*, Surg. Clin. North. Am., 1989, 69 (1), 31–40

[37] WANG B., HE Y.Y., NIE B.B., XU S.C., ZHANG J.H., *Abdominal injury of vehicle occupant in underbody blast events*, Journal of Jilin University, 2021, 51 (3), 792–798.

[38] WANG B., YANG J.B., YAO L.G., HE Y.Y., LYU H.Y., TANG J.S., XU S.C., ZHANG J.H., *Blast injuries to human lung induced by blast shock waves*, Explosion and Shockwaves, 2022, 42 (12), 13–21.

[39] WATTS S., KIRKMAN E., BIELER D., BJARNASON S., FRANKE A., GUPTA R., LEGGIERI M.J. JR., ORRU H., OUELLET S., PHILIPPENS M., SARRON J.-C., SKRIUDALEN S., TELAND J.A., RISLING M., CERNAK I., *Guidelines for using animal models in blast injury research*, J. R. Army Med. Corps., 2019, 165 (1), 38–40.

[40] YEN R.T., FUNG. C., HO H.H., BUTTERMAN G., *Speed of stress wave propagation in lung*, J. Appl. Physiol., 1986, 61 (1), 701–705.

[41] ZHANG S.X., WANG P.A., LIU Z.J., *Atlas of Chinese Visible Human (Male and Female)*, China Science Publishing and Media, Ltd., 2004.